PAPER

CrossMark
click for updates

Fe-doped Beta zeolite from organotemplate-free synthesis for NH₃-SCR of NOₓ†

Yongjun Zhu,[a] Bingbing Chen,[a] Rongrong Zhao,[a] Qi Zhao,[a] Hermann Gies,[b] Feng-Shou Xiao,[c] Dirk De Vos,[d] Toshiyuki Yokoi,[e] Xinhe Bao,[f] Ute Kolb,[g] Mathias Feyen,[h] Stefan Maurer,[h] Ahmad Moini,[i] Ulrich Müller,[h] Chuan Shi*[a] and Weiping Zhang*[a]

Two types of Beta zeolites, one from organotemplate-free synthesis with a Si/Al ratio of 9 and the other from a commercial one with a Si/Al ratio of 19, were employed here to dope Fe for NH₃-SCR of NOₓ. Fe-Beta (Si/Al = 9) exhibits much higher activity than Fe-Beta (Si/Al = 19), especially at low-temperature regions (<250 °C). In addition, it also exhibits better hydrothermal stability as compared with Fe-Beta (Si/Al = 19), which demonstrates that it is a promising SCR catalyst with good activity as well as hydrothermal stability. The correlation between the quantitative calculation of the content of isolated Fe^{3+} in Beta zeolites and the NO conversion rate at 150 °C shows a linear relationship, suggesting that the isolated Fe^{3+} species affect the SCR activity directly. The higher activity of the Fe-Beta-9 catalyst is supposed to be related not only to the isolated Fe^{3+} but also to the acidity. Furthermore, the template-free synthesized Beta zeolite shows less dealumination during hydrothermal aging and therefore better hydrothermal stability during the SCR reaction.

1. Introduction

Selective catalytic reduction (SCR) by urea or ammonia (NH₃) is one of the most commonly applied technologies for abatement of nitrogen oxides (NOₓ) in oxygen excess.[1–3] After the first generation SCR catalysts based on vanadia supported on titania are realized, second generation ones based on transition metal ions in zeolite structures have emerged as promising SCR catalysts. Metal ion-exchanged zeolites, particularly doped with copper or iron, represent over 80% of the recent work on NH₃-SCR.[4,5]

Copper-exchanged ZSM-5 zeolites exhibit good activities for NH₃-SCR of NOₓ, but the ZSM-5 zeolite has poor hydrothermal stability due to dealumination.[6] SSZ-13 zeolite with smaller pore size and better hydrothermal stability was found to be a better support for copper to obtain a good SCR catalyst, which has found many applications in diesel engine exhaust treatment.[7] However, Cu-zeolite catalysts have the problem of deterioration upon exposure to sulfur-containing gases.[8] It is known that Fe-exchanged zeolites have better tolerance to sulfur as compared with Cu-zeolites.[9–13] However, due to the small pore size of the SSZ-13 zeolite, it is difficult to achieve a large amount of iron at the exchange sites, which has been regarded to be important for SCR reaction.[14]

The chemical composition of Fe-zeolites and the structure of iron have been extensively investigated using EPR, UV-vis and EXAFS, *etc.* A variety of Fe species are identified, including isolated Fe species, oligomers of varying nuclearity and α-Fe_2O_3 particles that coexisted.[15–18] However, their catalytic functions during the SCR reaction are still under discussion. As pointed out by Brandenberger *et al.*,[19] the SCR activity was observed to be primarily caused by monomeric iron sites at temperatures below 300 °C; at T > 300 °C, the contributions

[a] *State Key Laboratory of Fine Chemicals, School of Chemistry, Dalian University of Technology, Dalian 116024, China. E-mail: chuanshi@dlut.edu.cn, wpzhang@dlut.edu.cn; Tel: +86 411 84986083, +86 411 84986326*

[b] *Institut für Geologie, Mineralogie und Geophysik, Ruhr-Universität Bochum, Germany*

[c] *Department of Chemistry, Zhejiang University, Hangzhou 310028, China*

[d] *Centre for Surface Chemistry and Catalysis, K.U. Leuven, Leuven, Belgium*

[e] *Chemical Resources Laboratory, Tokyo Institute of Technology, Yokohama, Japan*

[f] *State Key Laboratory of Catalysis, Dalian Institute of Chemical Physics, Dalian 116023, China*

[g] *Institut für Physikalische Chemie, Johannes Gutenberg-Universität Mainz, 55128 Mainz, Germany*

[h] *BASF SE, Process Research and Chemical Engineering, 67056 Ludwigshafen, Germany*

[i] *BASF Corporation, Catalysts LLC, Iselin, NJ 08830, USA*

† Electronic supplementary information (ESI) available: EPR spectra of H-Beta-9 and H-Beta-19 catalysts measured at −196 °C, NH₃ conversion, N₂O yield and N₂ selectivity of both Fe-Beta-9 and Fe-Beta-19 series catalysts. Correlations of NO conversion at 550 °C as a function of clustered and bulk Fe species contents of Fe-Beta-9 and Fe-Beta-19 series catalysts. XRD patterns and one-dimensional ²⁷Al MAS NMR spectra of hydrothermally aged samples. NH₃-TPD profiles of the indicated catalysts with ammonia adsorbed at RT for 60 min. See DOI: 10.1039/c6cy00231e

This journal is © The Royal Society of Chemistry 2016

Catal. Sci. Technol., 2016, **6**, 6581–6592 | 6581

are from dimeric iron species, oligomeric species, and partially uncoordinated iron sites in the outermost layer of iron oxide particles; while Sachtler et al.[17,18] suggested that not all monomer sites were equally active in the SCR reaction. Two different types of iron monomers were identified, in which one has high symmetry and the other has low symmetry. They may contribute differently to the SCR reaction. Maier et al.[20] and Kim et al.[21] found that the bridging Fe–O–Fe dimers formed and were active in the NH_3-SCR reaction. However, it is still a big challenge to distinguish the active iron species from those of abundantly present spectator iron species, since the active iron species usually account for only a small portion of the total iron content.

Much less work has been done on Fe-Beta than on Fe-ZSM-5, although Fe-Beta has shown very interesting SCR activity.[22–25] In the present work, the Beta zeolite (Si/Al = 9) synthesized from the organotemplate-free approach was employed as a support to host the iron ions, which was compared with commercial Beta (Si/Al = 19) supported catalysts. Two interesting points are presented in this paper. The first one is the correlation between the catalyst's structure and activity in a simple feed of 500 ppm NO, 500 ppm NH_3, 10% O_2 and balance N_2 to clarify the nature of the higher activities of Al rich Beta supported Fe catalysts. The other one is from the point of view of application; the hydrothermal stability of these Fe-doped Beta catalysts was studied in the presence of both H_2O and CO_2. Different dealumination behaviors were observed. Although Al rich, the organotemplate-free synthesized Beta supported Fe catalysts exhibit even better hydrothermal stability, which make them promising SCR catalysts with good activity as well as hydrothermal stability.

2. Experimental

2.1 Catalyst preparation

Organotemplate-free Na-Beta zeolite with a Si/Al ratio of 9 was obtained from BASF, Germany, whose synthesis approach was reported elsewhere.[26] In brief, organotemplate-free synthesis of Beta zeolite was carried out in aluminosilicate gel with a molar ratio of 40 SiO_2/1 Al_2O_3/10 Na_2O/570 H_2O at a temperature of 140 °C for 17–19 h in the presence of calcined Beta zeolite seeds with particle sizes of 60–100 nm. Before employment, Na-Beta-9 underwent a conventional ion-exchange process for its NH_4 type. On the basis of NH_4-Beta-9, a series of different iron-containing zeolite catalysts were prepared by incipient wetness impregnation (IWI) with a solution of ferrocene in toluene at room temperature for 48 h. Subsequently, the resulting samples were calcined in air at 500 °C for 4 h with the heating rate of 4 °C min^{-1}. For comparison, the conventional Na-Beta zeolite (Si/Al ≈ 19, from Zeolyst) was also employed using identical preparation procedures. The catalysts were denoted as Fe(m)-Beta-(n), where m (wt%) stands for the Fe content determined by ICP, and n represents the Si/Al ratio.

For hydrothermal treatment, the Fe-Beta catalysts have been aged in 10% H_2O vapor/Ar at 750 and 850 °C for 10 h, respectively. The obtained catalysts were denoted as A(x)-Fe(m)-Beta-(n), where A(x) stands for hydrothermal aging at a certain temperature.

2.2 Catalyst characterization

The Fe contents in the catalysts were determined by inductively coupled plasma-atomic emission spectroscopy (ICP-AES, Optima 2000 DV, USA). The details are listed in Table S1, ESI.†

The powder X-ray diffraction (XRD) experiments were performed using an X-ray diffractometer (Rigaku D/Max 2400) with Cu Kα radiation (λ = 1.5404 Å) in a 2θ range of 5–50° at 0.02° s^{-1}.

UV-vis diffuse reflectance spectra were recorded in the range of 190–800 nm on a JASCO V-550 spectrometer equipped with an integrating sphere coated with $BaSO_4$. Deconvolution of the UV-vis spectra was conducted using DM software. The various iron species were quantified relative to each other by the area ratios of the corresponding sub-bands.[27]

Electron paramagnetic resonance (EPR) measurements were carried out at −196 °C using a Bruker ELEXSYS E500 spectrometer operating at the X band (~9.8 GHz). The magnetic field was modulated at 100 Hz, and the g value was determined from precise frequency and magnetic field values.

[57]Fe Mössbauer spectra were collected at room temperature and −196 °C using a spectrometer working in constant acceleration mode with a ^{57}Co:Rh source. Data catalysis involved a least-square fitting procedure assuming a Lorentzian peak shape and employing the fitting program MössWin 3.0 I. The isomer shift (IS) values were given relative to iron foil at room temperature.

All solid-state MAS NMR experiments were performed using the Agilent DD2-500 MHz spectrometer. ^{27}Al MAS NMR spectra were acquired at 130.2 MHz using a 4 mm MAS NMR probe with a spinning rate of 14 kHz. Chemical shifts were referenced to $(NH_4)Al(SO_4)_2$·12H_2O at ~0.4 ppm as a secondary reference. The spectra were accumulated for 200 scans with π/12 flip angle and 2 s pulse delay. ^{27}Al MQ MAS NMR spectra were collected using a three-pulse sequence incorporating a z-filter.[28–30] A two-dimensional Fourier transformation followed by a shearing transformation gave a pure absorption mode 2D contour plot. The second-order quadrupolar effect (P_Q) and isotropic chemical shift (δ_{iso}) values were calculated according to the procedure introduced in the reference.[30]

2.3 Catalytic activity measurements

The SCR activity measurements were carried out in a micro fixed-bed quartz reactor (i.d. 6 mm) with the reactant gas mixture containing 500 ppm NO, 500 ppm NH_3, 10% O_2 and balance N_2. The total flow rate was 400 ml min^{-1}, corresponding to a gas hourly space velocity (GHSV) of about 80, 000 h^{-1}. NO, NO_2, NO_x(=NO + NO_2), NH_3 and N_2O contents were monitored continuously using a NO_x analyzer (Ecophysics,

6582 | Catal. Sci. Technol., 2016, 6, 6581–6592

This journal is © The Royal Society of Chemistry 2016

Switzerland) and an NH_3/N_2O analyzer (Sick Maihak, Germany), respectively. To avoid errors caused by the conversion of ammonia in the analyzer, an ammonia trap containing phosphoric acid solution was installed upstream. All data were obtained when the SCR reaction reached a steady state at each temperature. The conversion of NO and NH_3 and the selectivity of N_2 were calculated as follows:[31–34]

$$X_{NO} = \frac{[NO]_{in} - [NO]_{out}}{[NO]_{in}} \times 100\% \qquad (1)$$

$$X_{NH_3} = \frac{[NH_3]_{in} - [NH_3]_{out}}{[NH_3]_{in}} \times 100\% \qquad (2)$$

$$S_{N_2} = \frac{[NO]_{in} - [NO]_{out} + [NH_3]_{in} - [NH_3]_{out} - [NO_2]_{out} - 2[N_2O]_{out}}{[NO]_{in} - [NO]_{out} + [NH_3]_{in} - [NH_3]_{out}} \times 100\% \qquad (3)$$

where $[NO]_{out}$ and $[NH_3]_{out}$ are the NO and NH_3 concentrations in the product gas stream [ppm] and $[NO]_{in}$ and $[NH_3]_{in}$ are the NO and NH_3 concentrations in the feed gas [ppm].

3. Results

3.1 Structure–performance correlations

3.1.1 Catalytic activities. Fig. 1(A) shows the activities of Fe-Beta-9 catalysts of various Fe contents for NH_3-SCR of NO_x. It is clear that the support H-Beta-9 itself is active for the SCR reaction, but good performance could only be achieved in a narrow temperature range of 350–500 °C. Similar results have been obtained by other groups; acidity may account for its catalytic performance.[27,35,36] In the literature, the role of Brønsted/Lewis acidity in the SCR reaction is rather controversial. In any case, the acidity could influence the reaction by NH_3 storage.[37] After doping of Fe, the Fe-Beta catalysts indicate highly improved NO conversions in the whole temperature range of 125–550 °C. For the Fe(0.2)-Beta-9 catalyst, NO conversion is 15% at 150 °C. With an increase in temperature, NO conversion increases and reaches *ca.* 95% at 450 °C. For the Fe(1.3)-Beta-9 catalyst, NO conversion is *ca.* 54% at temperatures as low as 150 °C and reaches *ca.* 90% at 200–500 °C. Upon further increasing the temperature, NO conversion decreases, which might be due to the occurrence of a side reaction such as NH_3 oxidation.[19,38] Upon further enhancement of Fe content to 2.1 and 5.4 wt%, NO conversion at low temperatures (such as 150 °C) does not increase that much, but the conversion at higher temperatures decreases with Fe loading. These results clearly demonstrate that Fe loading exerts opposite effects on the low and high temperature NO conversions. With an increase in Fe loading, NO conversions at low temperatures increase, but those at high temperatures decrease.

As a comparison, the activities of Fe-Beta-19 catalysts were also investigated under identical conditions, *cf.* Fig. 1(B). H-Beta-19 itself is also active in the SCR reaction. Besides the acidity, a trace amount of Fe impurity indicated by the EPR spectra of the support might also contribute to the SCR activity (Fig. S1 in the ESI†). A small amount of Fe (≤1.4 wt%) in the zeolite enhances the activity obviously. A further increase in Fe loading does not enhance the activities at low temperatures obviously but lowers the NO conversions at high temperatures. By comparing the NO conversion at a similar Fe loading, Fe-Beta-9 catalysts always exhibit much higher activities than Fe-Beta-19 catalysts.

In addition, as shown in Fig. S2 and S3 in the ESI,† the highest amount of N_2O yielded in the course of the NH_3-SCR process is much less than 20 ppm. Thus, it is clear that the Fe-Beta-9 and Fe-Beta-19 catalysts exhibit superior selectivity to N_2 (Fig. S4 in the ESI†).

3.1.2 Structure characterization. XRD patterns were collected over both fresh Fe-Beta-9 and Fe-Beta-19 series samples. As displayed in Fig. 2, the peaks at 2θ of 7.6, 13.4, 14.4, 21.2 and 22.2° are typical diffractions of the BEA framework structure.[8,26] There is no diffraction peak ascribed to any kind of crystal Fe phases like α-Fe_2O_3 observed even at a higher Fe loading of 5 wt%.

The EPR spectra recorded at −196 °C are shown in Fig. 3. Three signals are observed over Fe doped samples: one sharp peak at $g' = 4.3$ with a low field shoulder at $g' = 9.7$ and a broader peak at $g' = 2.0$. The signals at $g' = 4.3$ and 9.7 indicate the high spin Fe^{3+} ions with a highly distorted rhombic coordination geometry, which is due to the isolated paramagnetic iron monomers found at ion exchange positions inside the zeolite micropores.[27] The $g' = 2.0$ signal is probably a superposition of two signals where one is a sharp signal from axially distorted Fe^{3+} monomers and the other is a broad signal from the iron oxygen oligomers.[27,39] A method is suggested to discriminate between the two cases; the signal of the isolated Fe^{3+} is narrow and the intensity increases with a decrease in temperature; however, the signal of Fe_xO_y oligomers is often broad and the temperature dependence is always different to the paramagnetic behavior due to the intrinsic anti-ferromagnetic interaction.[40–43] Based on its peak broaden characteristics and its anti-ferromagnetic properties, we tentatively assigned the signal at about $g' = 2.0$ to Fe_xO_y oligomers. As can be seen in Fig. 3, with an increase in Fe loading, signals at $g' = 4.3$ and $g' = 2.0$ become more intense and could be clearly observed for samples with Fe loading higher than 1.0 wt%. It is noted that for a similar Fe loading over Fe-Beta-9 and Fe-Beta-19 there seems to be more oligomers formed over the Fe-Beta-19 series samples.
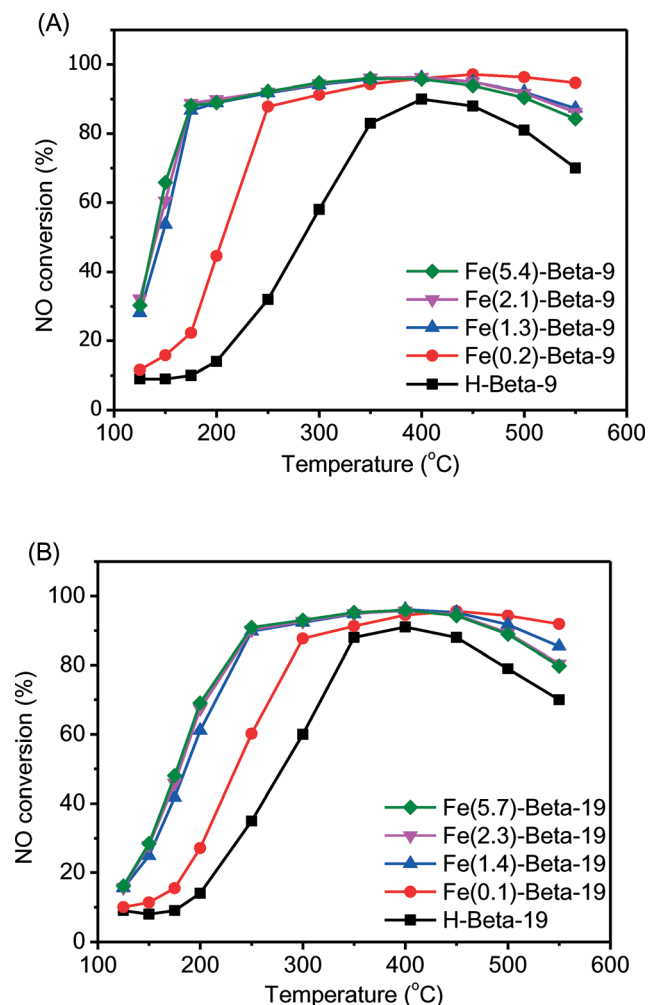
This journal is © The Royal Society of Chemistry 2016

Catal. Sci. Technol., 2016, **6**, 6581–6592 | **6583**

Fig. 1 NO conversions for Fe-Beta-9 (A) and Fe-Beta-19 (B) series catalysts as a function of temperature. Conditions: 500 ppm NO, 500 ppm NH$_3$, 10%O$_2$, balance N$_2$; GHSV = 80 000 h^{-1}.
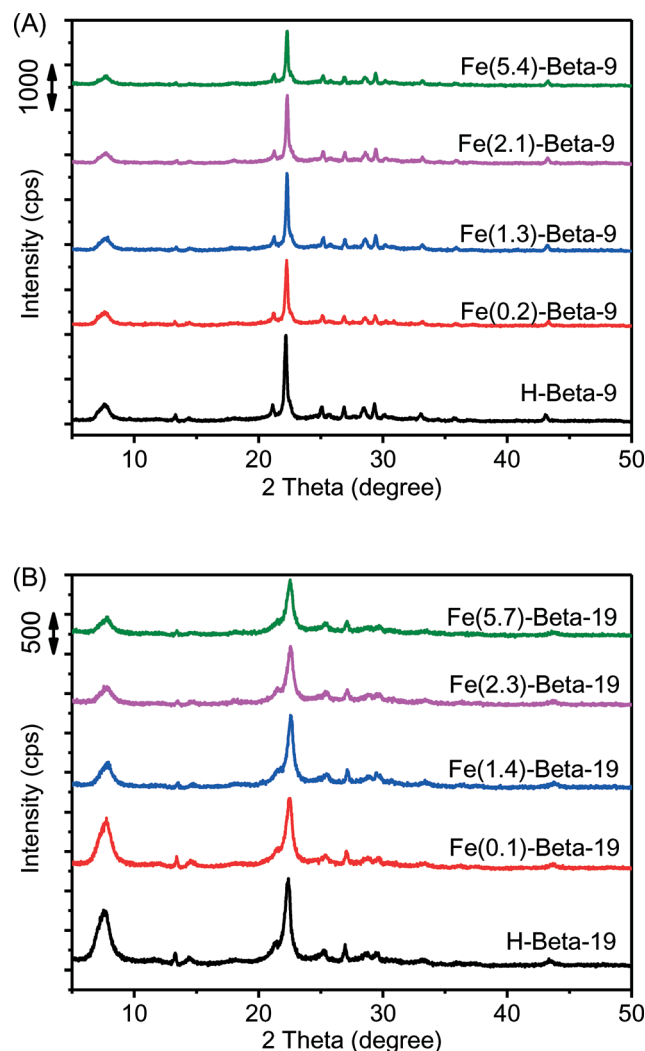

Fig. 2 XRD patterns of both Fe-Beta-9 (A) and Fe-Beta-19 (B) series catalysts.

Variable temperature ^{57}Fe Mössbauer spectra were used to detect Fe species; Fig. 4 and 5 show the spectra acquired at RT and −196 °C, respectively. The RT Mössbauer spectrum is dominated by an asymmetric doublet as shown in Fig. 4, implying contribution from more than one species. The key parameters obtained after fitting the experimental doublet data, *i.e.* isomer shift (IS, mm s^{-1}) and quadrupole splitting (QS, mm s^{-1}), are listed in Table 1. For the samples at RT, best fitting gives primarily two iron components, namely, the sharp doublet with IS = 0.34 mm s^{-1} and QS = 0.73 mm s^{-1} that is ascribed to the mononuclear Fe^{3+} (isolated Fe^{3+} at exchange sites) and the broad doublet with IS = 0.34 mm s^{-1} and QS = 1.1 mm s^{-1} that is assigned to the dimeric Fe^{3+} complexes.[44] The parameters demonstrated that both iron components are Fe^{3+} moieties, and there is no Fe^{2+} observed. The ^{57}Fe Mössbauer spectra recorded at −196 °C indicate a sextet type signal. By curve fitting, the obtained sub-bands representing two doublets and two sextets are clearly shown. The corresponding parameters are also summarized in Table 1. It is clear that doublet patterns of mononuclear Fe^{3+}

and dimeric Fe^{3+} species also appeared in the low-temperature Mössbauer spectra, with a little shift in IS. Apart from those patterns, a sextet pattern characterized by IS ≈ 0.2 mm s^{-1} and QS ≈ 0 mm s^{-1} is observed, which corresponded to Fe$_x$O$_y$ oligomers.[14,45,46] By comparing the data for Fe-Beta-9 and Fe-Beta-19, the spectral contribution from mononuclear and dimeric Fe^{3+} species is larger over the Fe(2.1)-Beta-9 sample compared with Fe(2.3)-Beta-19, indicating that more mononuclear and dimeric Fe^{3+} species appeared over the Fe-Beta zeolite synthesized from the organotemplate-free method.

UV-vis diffuse reflectance spectra were recorded for all fresh samples, as shown in Fig. 6. Usually, linear combination analysis of UV-vis spectra based on Gaussian/Lorentz functions to represent the different sub-bands found in the spectrum is used.[27] Generally, the bands below 300 nm were assigned to the isolated Fe ions; the bands between 300–400 nm are ascribed to small oligomeric Fe$_x$O$_y$ clusters, and the bands above 400 nm are ascribed to large Fe$_2$O$_3$ particles
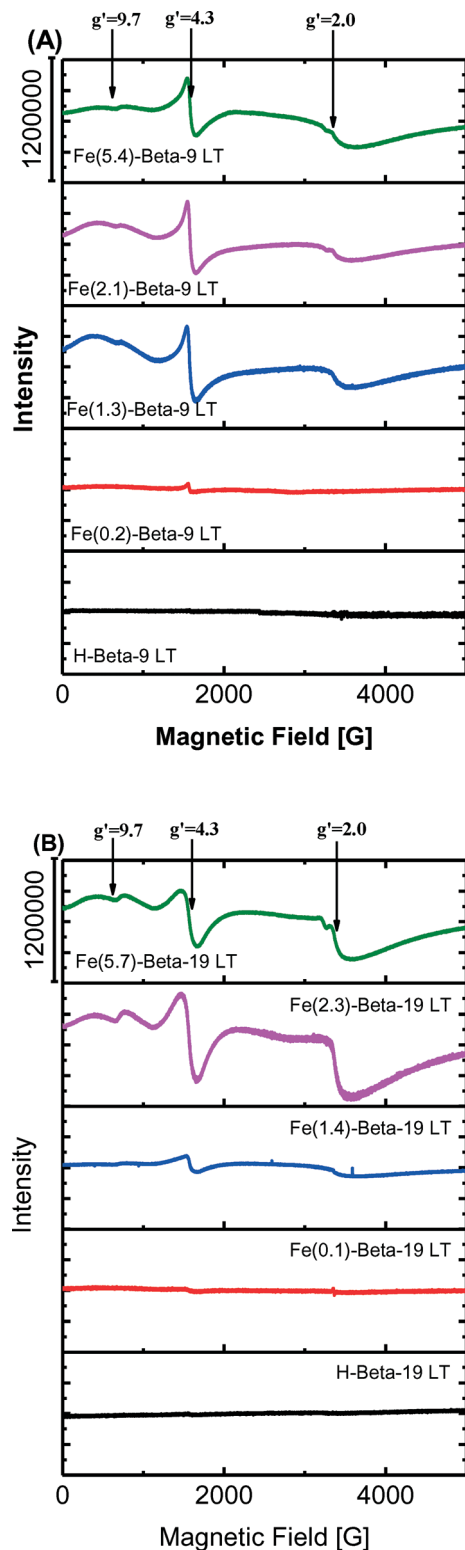
6584 | *Catal. Sci. Technol.*, 2016, **6**, 6581–6592

This journal is © The Royal Society of Chemistry 2016

Fig. 3 EPR spectra of both Fe-Beta-9 (A) and Fe-Beta-19 (B) series catalysts measured at −196 °C.

Fig. 4 ^{57}Fe Mössbauer spectra of both Fe(2.1)-Beta-9 (A) and Fe(2.3)-Beta-19 (B) catalysts at room temperature.

located at the external surface of the zeolite.[27,47] Table 2 summarizes the amount of various iron species derived from the intensity of the sub-bands, the relative percentage and the total iron contents in the samples. According to the results
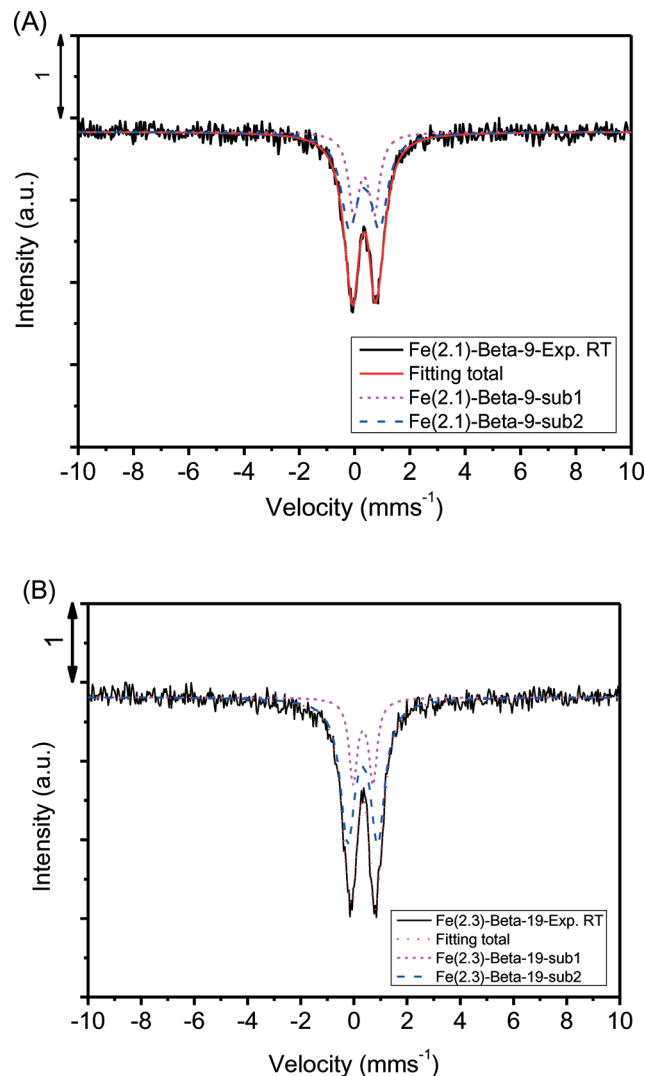
summarized for the Fe-Beta-9 samples, more than 90% of iron is in the form of isolated Fe^{3+} in Fe(0.2)-Beta-9, while the percentage reduces to 75% in Fe(1.3)-Beta-9. Furthermore, with a decrease in the relative percentage of isolated Fe^{3+}, the percentage of oligomeric Fe_xO_y clusters increases with incremental iron loading content. Similar trends are observed over Fe-Beta-19 series samples. However, by comparison of the distribution of different Fe species over Beta-9 and Beta-19 zeolites at an exact Fe loading, it is clear that more isolated Fe^{3+} species exist in Al-rich Beta-9, while more clustered Fe species are observed over Beta-19 zeolite. It should be noted that no matter for Fe-Beta-9 nor for Fe-Beta-19 samples, the relative percentage of bulk Fe species is the smallest, which is in accordance with the XRD measurements that there is no bulk α-Fe_2O_3 detected.

3.1.3 Correlations. To establish quantitative correlations between structure characterization and activity measurements, the content of the isolated Fe^{3+} species calculated from UV-vis measurements (as shown in Table 2) was
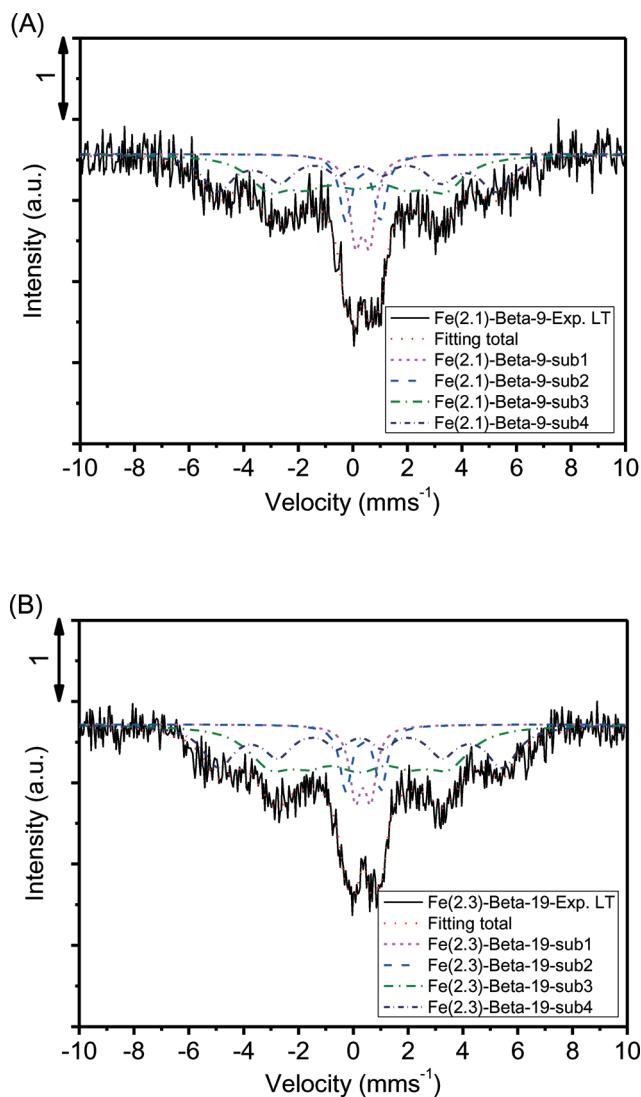
This journal is © The Royal Society of Chemistry 2016

Catal. Sci. Technol., 2016, **6**, 6581–6592 | **6585**

Fig. 5 ^{57}Fe Mössbauer spectra of both Fe(2.1)-Beta-9 (A) and Fe(2.3)-Beta-19 (B) catalysts at −196 °C.

version rate at 150 °C increased linearly from 0.074 to 0.54 μmol g_{cat}^{-1} s^{-1}. Similar results were obtained over Fe-Beta-19; with an increase in the isolated Fe^{3+} content from 0 to 203.6 μmol g_{cat}^{-1}, the NO conversion rate at 150 °C linearly increased from 0.066 to 0.23 μmol g_{cat}^{-1} s^{-1}. The results indicate that the isolated Fe^{3+} species affect the SCR activity directly. While with an increase in the amounts of clustered and bulk Fe species, the NO conversion at 550 °C decreased apparently (as shown in Fig. S5†). This should be ascribed to the side reaction of NH_3 oxidation catalyzed by Fe_xO_y clustered and bulk Fe species, which leads to the decreased NO conversion at high temperatures.[19]

3.2 Effects of hydrothermal treatment

3.2.1 Activities. The activities of Fe-Beta zeolites after hydrothermal treatment in 10% H_2O at 750 °C and 850 °C for NH_3-SCR of NO_x in the presence of 5% H_2O and 10% CO_2 are shown in Fig. 8. As compared with those obtained in the absence of H_2O and CO_2 (Fig. 1), NO conversion is hardly affected by the introduction of H_2O and CO_2 in the feed over Fe-Beta zeolites. The hydrothermal treatment of Fe(2.3)-Beta-9 at 750 °C does not decrease the activity apparently. However, after treatment at 850 °C, NO conversion at low temperatures obviously decreased, from 88% to 65% at 200 °C. For Fe(2.3)-Beta-19, even upon hydrothermal treatment at 750 °C, the conversions at low temperatures (<300 °C) decrease apparently, and treatment at 850 °C further decreased the activity. It is generally believed that the Al-rich zeolite has poor hydrothermal stability probably due to easier dealumination. However, the present results show that Fe-Beta-9 synthesized from the organotemplate-free method with a lower Si/Al ratio exhibits even better hydrothermal stability compared with Fe-Beta-19 from the commercial zeolite.

3.2.2 Structural changes. The XRD patterns for the hydrothermal treated samples are shown in Fig. S6 in the ESI.† As compared with the fresh sample, there is no framework collapse for Beta zeolites observed. Meanwhile, there is no different peak ascribed to any kind of crystal α-Fe_2O_3 observed, even after hydrothermal treatment at 850 °C.

correlated with the reaction rate at 150 °C, as shown in Fig. 7. It is clear that with an increase in the isolated Fe^{3+} content from 0 to 289.3 μmol g_{cat}^{-1} for Fe-Beta-9, the NO con-

Table 1 ^{57}Fe Mössbauer parameters of Fe-Beta series catalysts at room temperature and at −196 °C

Catalysts	Isomer shift^a (mm s^{-1})	QS^b (mm s^{-1})	Magnetic field (T)	Spectral contribution^c (%)	Subspectra and Fe sites
Fe(2.1)-Beta-9	0.34	1.08		63.9	Fe^{3+}–O–Fe^{3+}
	0.34	0.73		36.1	Isolated Fe^{3+}
Fe(2.3)-Beta-19	0.33	1.13		74.4	Fe^{3+}–O–Fe^{3+}
	0.34	0.74		25.6	Isolated Fe^{3+}
Fe(2.1)-Beta-9^d	0.36	0.52		14.8	Isolated Fe^{3+}
	0.37	1.26		12.2	Fe^{3+}–O–Fe^{3+}
	0.21	−0.13	31.6	34.1	Fe_xO_y oligomers
Fe(2.3)-Beta-19^d	0.36	0.56		10.9	Isolated Fe^{3+}
	0.37	1.29		10.4	Fe^{3+}–O–Fe^{3+}
	0.25	0.02	32.1	34.8	Fe_xO_y oligomers

^{a} Isomer shift, relative to α-Fe at room temperature. ^{b} Quadrupole splitting, electric quadrupole splitting. ^{c} Relative resonance areas of the different components of the absorption patterns. ^{d} Measured at −196 °C.
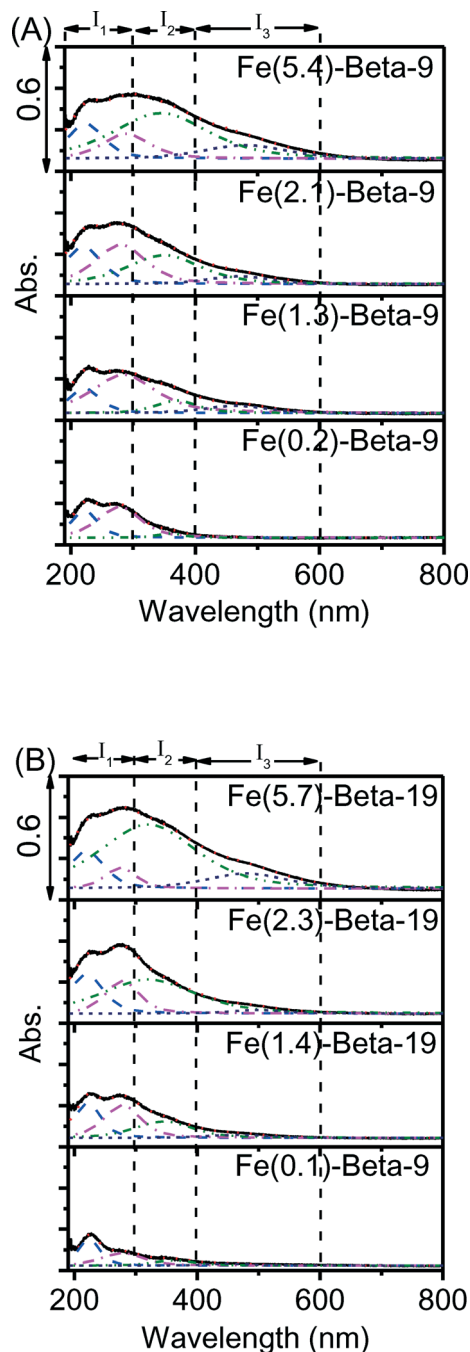
Fig. 6 UV-vis DR spectra of both Fe-Beta-9 (A) and Fe-Beta-19 (B) series catalysts.

The hydrothermally aged samples are further characterized by EPR at −196 °C as shown in Fig. 9. Similar to those observed in Fig. 3 for the unaged samples, there are three signals observed with $g' = 4.3$ and $g' = 9.7$ ascribed to the isolated Fe^{3+} ions and $g' = 2.0$ assigned to the Fe_xO_y oligomers. It is clearly shown that after hydrothermal treatment, the intensity of the signal due to the isolated Fe^{3+} greatly decreases, indicating the loss of the isolated Fe^{3+} species upon hydrothermal treatment. Meanwhile, the increase in peak intensity due to Fe_xO_y oligomers is obvious, indicating the ag-

gregation of Fe species from the isolated to the clustered ones.[48–50] A special case is observed over Fe(2.3)-Beta-19 aged at 850 °C. The signal at $g' \approx 2.0$ becomes very weak. This might be due to the intrinsic anti-ferromagnetic properties of Fe aggregates. Upon hydrothermal aging, the anti-ferromagnetic properties become dominant.[40–43]

The structural changes of Fe species upon hydrothermal treatment were further characterized by UV-vis spectroscopy as shown in Fig. 10. By curve fitting, the results are summarized in Table 2. It is obvious that the relative percentage of the isolated Fe^{3+} decreases, while the percentage of the oligomeric Fe_xO_y clusters and bulk Fe species increases with an increase in hydrothermal treatment temperature. The results indicate that the aggregation of Fe species occurs upon hydrothermal treatment as indicated by the decreased amount of isolated Fe^{3+} species accompanied by the increased amount of clustered and bulk Fe species. Even after treatment at 850 °C, the bulk Fe species still accounts for the smallest part of the whole species, which is consistent with the XRD measurements.

The one-dimensional ^{27}Al MAS NMR spectra are shown in Fig. S7 in the ESI.† As demonstrated, the peak at 54 ppm can be unambiguously assigned to the tetrahedrally coordinated framework aluminum Al(IV) in the H-Beta zeolite, while that at −3 ppm arises from the octahedrally coordinated Al designated as Al(VI).[29] The signal centered at about 30 ppm could be ascribed to the pentahedral Al(V).[51] Upon hydrothermal treatment, the peak intensity at 54 ppm decreases further, and that at −3 ppm increases. Meanwhile, the signal at around 30 ppm becomes more obvious. It is clear that dealumination occurs much severer in the Fe-Beta-19 catalyst than in the Fe-Beta-9 catalyst with hydrothermal aging. However, it is difficult to separate the contribution of aluminum with different isotropic shifts and quadrupolar coupling constants in the one-dimensional ^{27}Al MAS NMR spectra; one possibility is to use the two-dimensional multiple quantum technique. The two-dimensional ^{27}Al MAS NMR spectra are shown in Fig. 11. Different from the commercial H-Beta-19 zeolite shown in Fig.11(B), in which at least two groups of crystallographically distinct T sites exist in the H-Beta framework, only one signal appears in the 50–60 ppm region attributed to tetrahedrally coordinated aluminum species in the template-free H-Beta-9 zeolite (cf. Fig.11(A)).This means that this large amount of aluminum occupies only a restricted number of T sites. In line with the one-dimensional ^{27}Al MAS NMR after introducing Fe species, the intensities of extraframework aluminum species increase notably. Table 3 lists the isotropic chemical shifts (δ_{iso}) and quadrupolar parameters (P_Q). It is found that another type of tetrahedral framework Al(IV)$_b$ species with a large quadrupolar interaction of 7.4–7.6 MHz appears in the Fe-Beta catalyst. This large anisotropic quadrupolar broadening makes it difficult to be identified in the usual ^{27}Al MAS NMR spectra; however, it is clearly noticeable in the isotropic F1 projection. The introduction of Fe species leads to the formation of a second

This journal is © The Royal Society of Chemistry 2016

Catal. Sci. Technol., 2016, 6, 6581–6592 | 6587

Table 2 Numerical analysis of UV-vis spectra of Fe-Beta series catalysts. Percentage of the sub-bands (I_1: $\lambda < 300$ nm, I_2: $300 < \lambda < 400$ nm, I_3: $\lambda > 400$ nm) and wt% Fe of the corresponding species

Catalysts	Fe species						Catalysts	Fe species					
	Isolated		Clustered		Bulk			Isolated		Clustered		Bulk	
	I_1/%	wt%	I_2/%	wt%	I_3/%	wt%		I_1/%	wt%	I_2/%	wt%	I_3/%	wt%
H-Beta-9	—	—	—	—	—	—	H-Beta-19	—	—	—	—	—	—
Fe(0.2)-Beta-9	94	0.19	6	0.01	—	—	Fe(0.1)-Beta-19	77	0.07	16	0.02	7	0.01
Fe(1.3)-Beta-9	75	0.98	13	0.17	12	0.15	Fe(1.4)-Beta-19	64	0.89	30	0.42	6	0.09
Fe(2.1)-Beta-9	54	1.13	37	0.78	9	0.19	Fe(2.3)-Beta-19	42	0.97	54	1.24	4	0.09
Fe(5.4)-Beta-9	30	1.62	55	2.97	15	0.81	Fe(5.7)-Beta-19	20	1.14	66	3.76	14	0.80
A750-Fe(2.1)-Beta-9	51	1.07	42	0.88	7	0.15	A750-Fe(2.3)-Beta-19	35	0.81	56	1.29	9	0.20
A850-Fe(2.1)-Beta-9	41	0.86	47	0.99	12	0.25	A850-Fe(2.3)-Beta-19	33	0.76	59	1.36	8	0.19

Al(IV)$_b$ and Al(VI)$_b$ at the expense of Al(IV)$_a$, which indicates that Fe species may be associated with part of framework aluminum and located at the exchange sites of the Beta zeolite. After hydrothermal aging, pentahedral non-framework Al species appears clearly for all catalysts. Moreover, a strong octahedral nonframework Al(VI)$_b$ appears in Fe-Beta-19 aged at 850 °C, indicating much severer dealumination in the Fe-Beta-19 catalyst. Even under such severe hydrothermal treatment, the tetrahedral framework Al(IV)$_b$ signal can still be detected in the ^{27}Al MQ MAS NMR spectra. Thus, Al-rich Fe-Beta-9 has better hydrothermal stability than the Fe-Beta-19 catalyst.

4. Discussion

Two types of Beta zeolites were employed here to support Fe for NH_3-SCR of NO_x. Fe loading exerts opposite effects on low temperature and high temperature activities for Fe-Beta series catalysts. At low temperatures (<200 °C), NO conversions increased apparently with increasing Fe loading, while those at high temperatures (>450 °C) were decreased upon increment of Fe loading. The characterization of Fe species by

EPR, ^{57}Fe Mössbauer spectra and UV-vis indicates that there are three types of Fe species: isolated Fe^{3+} species, Fe_xO_y clustered species and α-Fe_2O_3 bulk species. With increasing
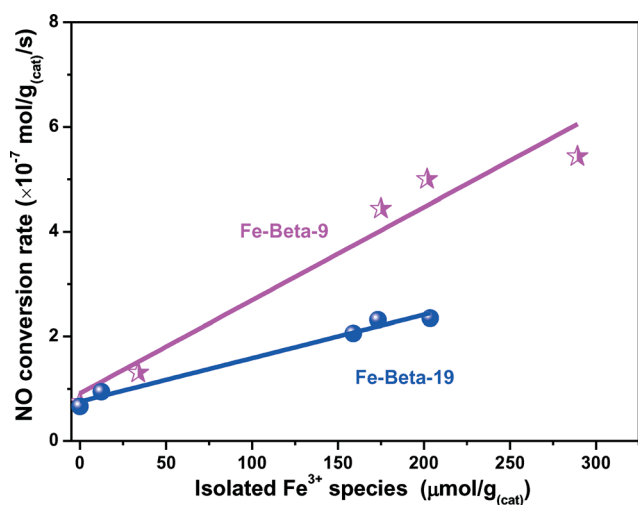
(A)

Fig. 7 Correlations of the NO conversion rate at 150 °C with the content of isolated Fe^{3+} species for Fe-Beta-9 and Fe-Beta-19 catalysts.
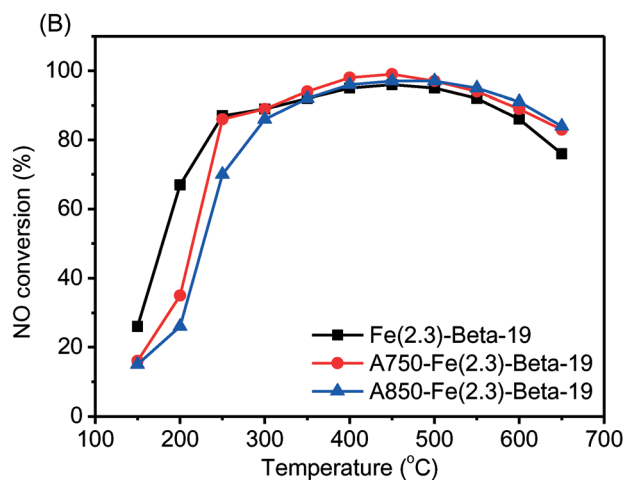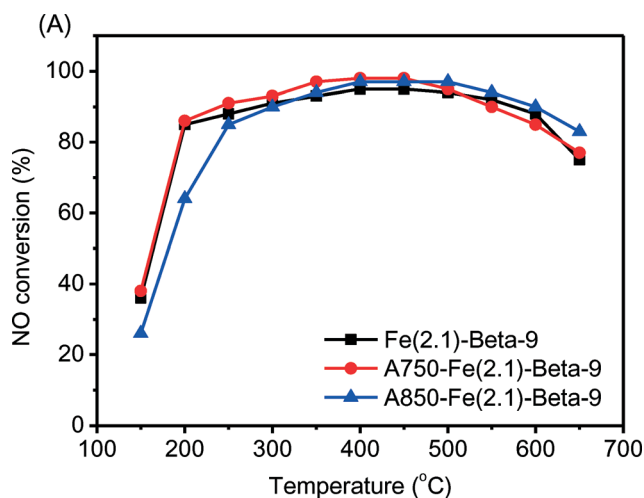
(B)

Fig. 8 NO conversion for Fe(2.1)-Beta-9 (A) and Fe(2.3)-Beta-19 (B) samples after hydrothermal treatment as a function of temperature. Conditions: NO 500 ppm, NH_3 500 ppm, O_2 10%, CO_2 10%, H_2O vapor 5%, balance N_2; GHSV = 80 000 h^{-1}.

6588 | *Catal. Sci. Technol.*, 2016, **6**, 6581–6592

This journal is © The Royal Society of Chemistry 2016

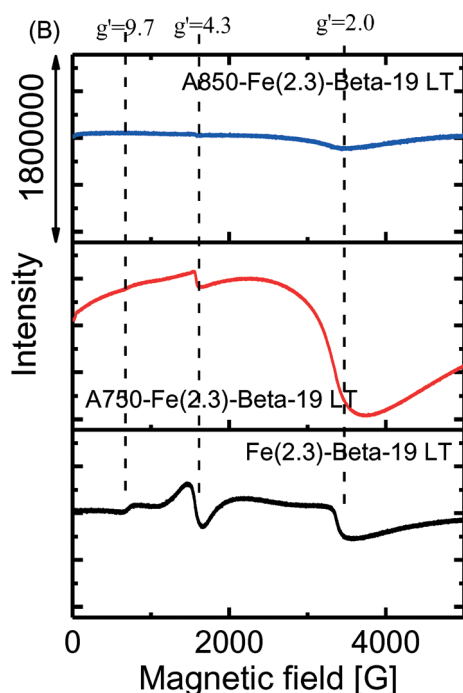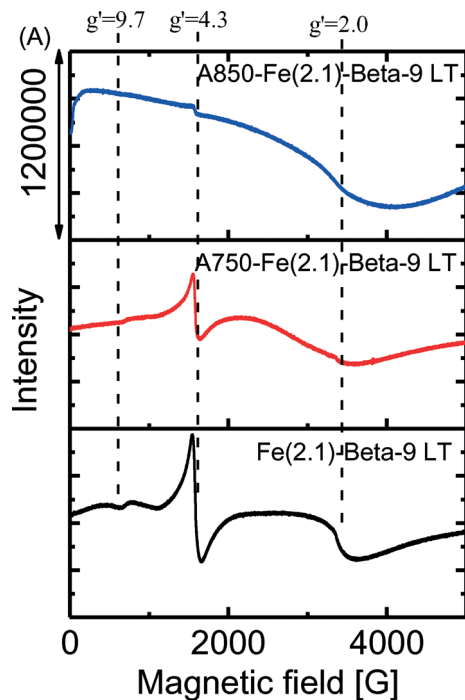**Fig. 9** EPR spectra of Fe-Beta-9 (A) and Fe-Beta-19 (B) series catalysts after hydrothermal treatments measured at −196 °C.

Fig. 10 UV-vis DR spectra of Fe(2.1)-Beta-9 (A) and Fe(2.3)-Beta-19 (B) series catalysts after hydrothermal treatments.

amount of Fe in the zeolite, the relative percentage of isolated Fe^{3+} decreases, but those of clustered and bulk Fe_xO_y species increase. By correlating this structural changes with the NO conversion rate at 150 °C as shown in Fig. 7, it is clear that with an increase in the isolated Fe^{3+} content in the

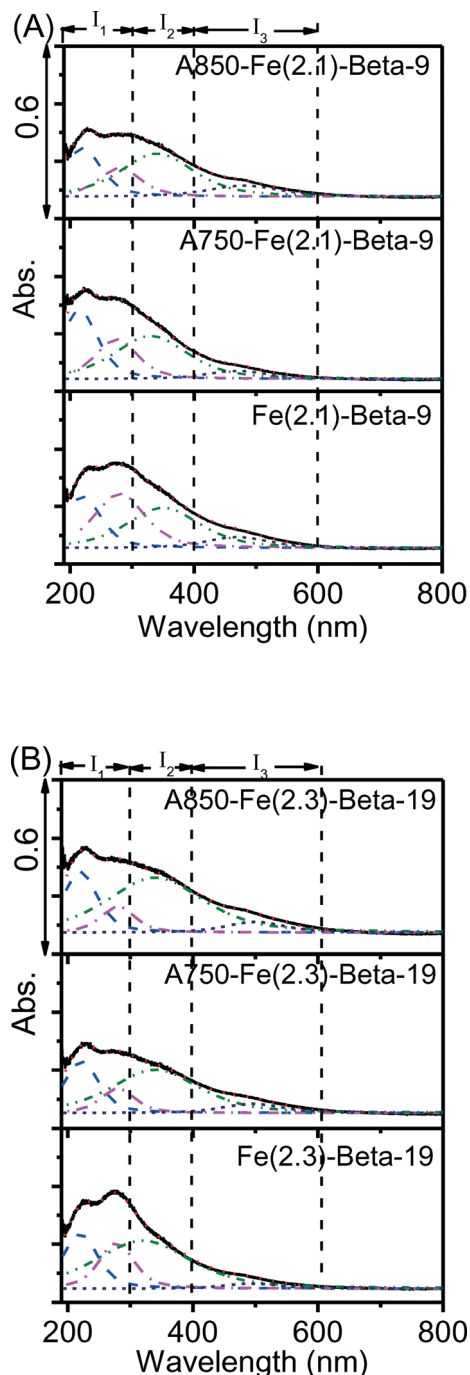Beta zeolite, the reaction rate at 150 °C increases linearly. The results indicate that the isolated Fe^{3+} species affect the SCR activity directly.

It is worth noting that the correlations were not on the same line for Fe-Beta-9 and Fe-Beta-19 catalysts; a higher slope was obtained over the Fe-Beta-9 catalyst. Such results suggest that not only the content of the isolated Fe^{3+} affects the SCR activity but also other factors. The Fe-Beta-9 zeolite possesses a higher amount of acidity as compared with
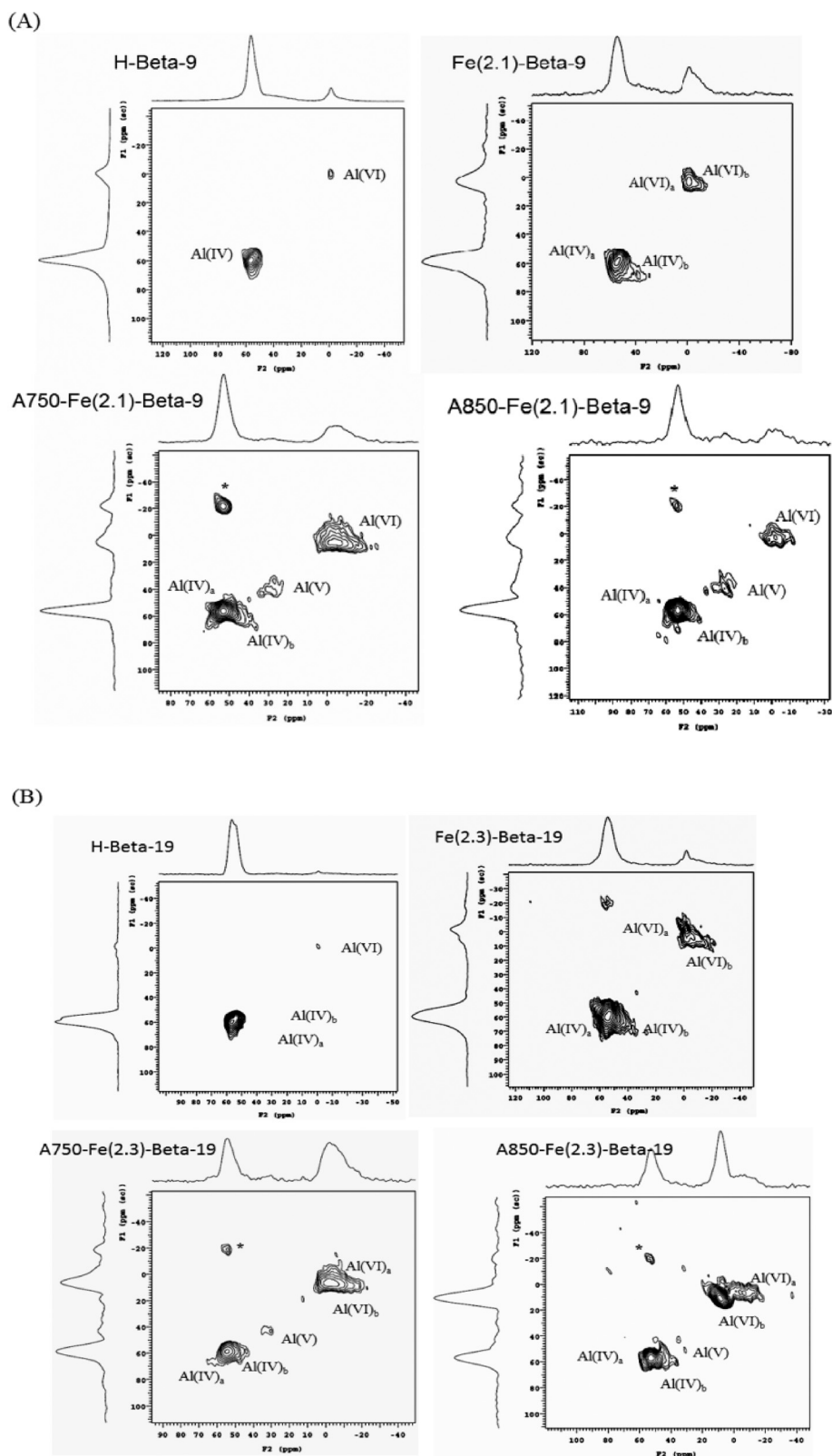
This journal is © The Royal Society of Chemistry 2016

Catal. Sci. Technol., 2016, **6**, 6581–6592 | **6589**

Paper

Catalysis Science & Technology

Fig. 11 ^{27}Al MQ MAS NMR spectra of Fe(2.1)-Beta-9 (A) and Fe(2.3)-Beta-19 (B) catalysts after hydrothermal treatments.

Fe-Beta-19, as shown by NH$_3$-TPD (Fig. S8†). As it has been revealed in many reports, acidity is involved in NH$_3$ adsorption and activation during the NH$_3$-SCR reaction.[52,53] The higher

activity of the Fe-Beta-9 catalyst might be related not only to the isolated Fe^{3+} but also to the acidity, which follows a bi-functional mechanism for NH$_3$-SCR of NO$_x$.[54,55] NH$_3$ was

6590 | *Catal. Sci. Technol.*, 2016, **6**, 6581–6592

This journal is © The Royal Society of Chemistry 2016

Table 3 NMR parameters determined from ^{27}Al MQ MAS NMR for Fe-Beta catalysts

Catalysts	Al(IV)$_a$	Al(IV)$_b$	Al(v)	Al(VI)$_a$	Al(VI)$_b$
H-Beta-9	58.7^a (2.5)^b			−0.3 (1.4)	
Fe(2.1)-Beta-9	57.3 (2.8)	57.4 (7.4)		1.6 (2.6)	−2.3 (4.3)
A750-Fe(2.1)-Beta-9	55.3 (2.4)	53.9 (6.4)	36.9 (4.6)	2.1 (4.3)	
A850-Fe(2.1)-Beta-9	55.8 (2.5)	55.5 (6.3)	35.7 (5.1)	1.3 (2.8)	
H-Beta-19	58.7 (2.4)	55.8 (2.6)		0.4 (1.6)	
Fe(2.3)-Beta-19	58.1 (3.2)	57.2 (7.6)		−0.9 (0.9)	0.7 (4.4)
A750-Fe(2.3)-Beta-19	57.1 (2.4)	54.2 (5.5)	39.2 (4.7)	2.1 (5.1)	4.1 (4.1)
A850-Fe(2.3)-Beta-19	55.7 (2.9)	51.7 (6.5)	42.1 (4.8)	2.3 (4.7)	10.1 (2.2)

^{a} δ_{iso} (ppm). ^{b} P_Q (MHz).

activated by the acid sites, and NO oxidation to NO$_2$ was catalyzed by the isolated Fe^{3+}; its synergy makes Fe-Beta-9 an excellent catalyst for NH$_3$-SCR reaction.

By comparison with the literature data, our results (Table S2†) show that the reaction rate of Fe(2.1)-Beta-9 at 125 °C is 0.27 μmol g$_{cat}^{-1}$ s^{-1}, and that at 150 °C is 0.50 μmol g$_{cat}^{-1}$ s^{-1}, which makes it one of the most active Fe-Beta catalysts for low temperature NH$_3$-SCR of NO$_x$.

Moreover, although Fe-Beta-9 catalysts are Al-rich, their hydrothermal stability is quite good. The characterization of the framework changes of the Beta zeolite support by ^{27}Al MAS NMR indicates that upon hydrothermal aging under the same conditions, there is always more severe dealumination that occurred over commercial Beta-19 as compared with the template-free Beta-9 zeolite. This might be due to the two types of framework Al that appeared in the commercial Beta, one of which might be unstable during the hydrothermal treatment. Accordingly, isolated Fe^{3+} species associated with the framework Al could be aggregated into Fe$_x$O$_y$ clusters and/or bulk species due to dealumination. As has been proved in the above results, the isolated Fe^{3+} species play key roles in the SCR reaction. The decrease in isolated Fe^{3+} species leads to the decreased activity for the SCR reaction. Hydrothermal treatment at 850 °C leads to much more severe dealumination of Fe-Beta-19 and therefore obvious loss of SCR activity for NH$_3$-SCR of NO$_x$.

5. Conclusions

As to catalysis over the Fe doped organotemplate free synthesized Beta zeolite for NH$_3$-SCR of NO$_x$, there are two interesting points presented in this paper. The first one is the structure–performance correlation studies. It is suggested that the content of isolated Fe^{3+} in the Beta zeolite affects the SCR activity directly. The higher activity of the Fe-Beta-9 catalyst is supposed to be related not only to the isolated Fe^{3+} but also to the acidity. The other one is that the organotemplate-free synthesized Beta zeolite shows less dealumination during hydrothermal aging and therefore better hydrothermal stability. In contrast, due to more severe dealumination of Fe-Beta-19 catalysts during hydrothermal treatment, the SCR activities decrease more apparently. Our results indicate that this organotemplate-free synthesized Beta shows more promise for future use as supports for SCR catalysts.

Acknowledgements

References

1 F. J. H. Bosh, *Catal. Today*, 1988, **2**, 369–379.
2 M. Schneider, U. Scharf, A. Wokaun and A. Baiker, *J. Catal.*, 1994, **150**, 284–300.
3 G. Qi, R. T. Yang and R. Chang, *Appl. Catal., B*, 2004, **51**, 93–106.
4 R. Nedyalkova, S. Shwan, M. Skoglundh and L. Olsson, *Appl. Catal., B*, 2013, **138**, 373–380.
5 K. Kamasamudram, N. Currier, T. Szailer and A. Yezerets, *SAE Int. J. Fuels Lubr.*, 2010, **3**, 664–672.
6 J. Y. Yan, G. D. Lei, W. M. H. Sachtler and H. H. Kung, *J. Catal.*, 1996, **161**, 43–54.
7 J. H. Kwak, R. G. Tonkyn, D. H. Kim, J. Szanyi and C. H. F. Peden, *J. Catal.*, 2010, **275**, 187–190.
8 L. Xu, C. Shi, Z. Zhang, H. Gies, F.-S. Xiao, D. De Vos, T. Yokoi, X. Bao, M. Feyen, S. Maurer, B. Yilmaz, U. Müller and W. Zhang, *Microporous Mesoporous Mater.*, 2014, **200**, 304–310.
9 X. B. Feng and W. K. Hall, *J. Catal.*, 1997, **166**, 368–376.
10 X. Feng and W. K. Hall, *Catal. Lett.*, 1996, **41**, 45–46.
11 H. Y. Chen and W. M. H. Sachtler, *Catal. Today*, 1998, **42**, 73–83.
12 P. Balle, B. Geiger and S. Kureti, *Appl. Catal., B*, 2009, **85**, 109–119.
13 Z. Liu, P. J. Millington, J. E. Bailie, R. R. Rajaram and J. A. Anderson, *Microporous Mesoporous Mater.*, 2007, **104**, 159–170.
14 F. Gao, M. Kollár, R. K. Kukkadapu, N. M. Washton, Y. Wang, J. Szanyi and C. H. F. Peden, *Appl. Catal., B*, 2015, **164**, 407–419.
15 D. E. Doronkin, A. Y. Stakheev, A. V. Kucherov, N. N. Tolkachev, G. O. Bragina, G. N. Baeva, P. Gabrielsson, I.

This journal is © The Royal Society of Chemistry 2016

Catal. Sci. Technol., 2016, **6**, 6581–6592 | **6591**

Gekas and S. Dahl, *Mendeleev Commun.*, 2007, **17**, 309–310.

16 A. V. Kucherov and M. Shelef, *J. Catal.*, 2000, **195**, 106–112.

17 E. M. El-Malki, R. A. van Santen and W. M. H. Sachtler, *J. Catal.*, 2000, **196**, 212–223.

18 T. V. Voskoboinikov, H. Y. Chen and W. M. H. Sachtler, *Appl. Catal., B*, 1998, **19**, 279–287.

19 S. Brandenberger, O. Krocher, A. Tissler and R. Althoff, *Appl. Catal., B*, 2010, **95**, 348–357.

20 S. M. Maier, A. Jentys, M. Janousch, J. A. van Bokhoven and J. A. Lercher, *J. Phys. Chem. C*, 2012, **116**, 5846–5856.

21 J. Kim, A. Jentys, S. M. Maier and J. A. Lercher, *J. Phys. Chem. C*, 2012, **117**, 986–993.

22 S. Shwan, J. Jansson, L. Olsson and M. Skoglundh, *Appl. Catal., B*, 2014, **147**, 111–123.

23 M. Muller, G. Harvey and R. Prins, *Microporous Mesoporous Mater.*, 2000, **34**, 135–147.

24 B. Yilmaz, U. Muller, M. Feyen, S. Maurer, H. Zhang, X. Meng, F. S. Xiao, X. Bao, W. Zhang, H. Imai, T. Yokoi, T. Tatsumi, H. Gies, T. De Baerdemaeker and D. De Vos, *Catal. Sci. Technol.*, 2013, **3**, 2580–2586.

25 P. Sazama, B. Wichterlová, Š. Sklenák, V. I. Parvulescu, N. Candu, G. Sádovská, J. Dědeček, P. Klein, V. Pashkova and P. Šťastný, *J. Catal.*, 2014, **318**, 22–33.

26 B. Xie, J. Song, L. Ren, Y. Ji, J. Li and F.-S. Xiao, *Chem. Mater.*, 2008, **20**, 4533–4535.

27 M. Hoj, M. J. Beier, J. D. Grunwaldt and S. Dahl, *Appl. Catal., B*, 2009, **93**, 166–176.

28 X. Li, W. Zhang, S. Liu, L. Xu, X. Han and X. Bao, *J. Phys. Chem. C*, 2008, **112**, 5955–5960.

29 X. J. Li, W. P. Zhang, S. L. Liu, L. Y. Xu, X. W. Han and X. H. Bao, *J. Catal.*, 2007, **250**, 55–66.

30 J. Rocha, C. Morais and C. Fernandez, in *New Techniques in Solid-State NMR*, ed. J. Klinowski, Springer Berlin Heidelberg, 2005, pp. 141–194.

31 W. P. Shan, F. D. Liu, H. He, X. Y. Shi and C. B. Zhang, *Catal. Today*, 2012, **184**, 160–165.

32 F. Liu, H. He, Y. Ding and C. Zhang, *Appl. Catal., B*, 2009, **93**, 194–204.

33 F. Liu, H. He, C. Zhang, Z. Feng, L. Zheng, Y. Xie and T. Hu, *Appl. Catal., B*, 2010, **96**, 408–420.

34 H. Z. Chang, X. Y. Chen, J. H. Li, L. Ma, C. Z. Wang, C. X. Liu, J. W. Schwank and J. M. Hao, *Environ. Sci. Technol.*, 2013, **47**, 5294–5301.

35 L. Ma, H. Chang, S. Yang, L. Chen, L. Fu and J. Li, *Chem. Eng. J.*, 2012, **209**, 652–660.

36 H. Liu, J. Wang, T. Yu, S. Fan and M. Shen, *Catal. Sci. Technol.*, 2014, **4**, 1350–1356.

37 F. Gao, N. M. Washton, Y. Wang, M. Kollár, J. Szanyi and C. H. F. Peden, *J. Catal.*, 2015, **331**, 25–38.

38 S. Brandenberger, O. Krocher, A. Tissler and R. Althoff, *Catal. Rev.: Sci. Eng.*, 2008, **50**, 492–531.

39 R. Q. Long and R. T. Yang, *J. Catal.*, 2000, **194**, 80–90.

40 R. Pérez Vélez, I. Ellmers, H. Huang, U. Bentrup, V. Schünemann, W. Grünert and A. Brückner, *J. Catal.*, 2014, **316**, 103–111.

41 E. Berrier, O. Ovsitser, E. V. Kondratenko, M. Schwidder, W. Grünert and A. Brückner, *J. Catal.*, 2007, **249**, 67–78.

42 J. Dedecek, D. Kaucky and B. Wichterlova, *Chem. Commun.*, 2001, 970–971.

43 J. Dedecek, D. Kaucky, B. Wichterlova and O. Gonsiorova, *Phys. Chem. Chem. Phys.*, 2002, **4**, 5406–5413.

44 K. A. Dubkov, N. S. Ovanesyan, A. A. Shteinman, E. V. Starokon and G. I. Panov, *J. Catal.*, 2002, **207**, 341–352.

45 J. Y. Wang, H. A. Xia, X. H. Ju, Z. C. Feng, F. T. Fan and C. Li, *J. Catal.*, 2013, **300**, 251–259.

46 J. B. Taboada, A. R. Overweg, P. J. Kooyman, I. Arends and G. Mul, *J. Catal.*, 2005, **231**, 56–66.

47 J. Perez-Ramirez, F. Kapteijn and A. Bruckner, *J. Catal.*, 2003, **218**, 234–238.

48 S. Shwan, R. Nedyalkova, J. Jansson, J. Korsgren, L. Olsson and M. Skoglundh, *Ind. Eng. Chem. Res.*, 2012, **51**, 12762–12772.

49 S. Shwan, J. Jansson, J. Korsgren, L. Olsson and M. Skoglundh, *Catal. Today*, 2012, **197**, 24–37.

50 S. Brandenberger, O. Krocher, M. Casapu, A. Tissler and R. Althoff, *Appl. Catal., B*, 2011, **101**, 649–659.

51 Z. W. Yu, A. M. Zheng, Q. A. Wang, L. Chen, J. Xu, J. P. Amoureux and F. Deng, *Angew. Chem., Int. Ed.*, 2010, **49**, 8657–8661.

52 P. S. Metkar, N. Salazar, R. Muncrief, V. Balakotaiah and M. P. Harold, *Appl. Catal., B*, 2011, **104**, 110–126.

53 E. Y. Choi, I. S. Nam and Y. G. Kim, *J. Catal.*, 1996, **161**, 597–604.

54 H. Schneider, S. Tschudin, M. Schneider, A. Wokaun and A. Baiker, *J. Catal.*, 1994, **147**, 5–14.

55 L. Wang, W. Li, S. J. Schmieg and D. Weng, *J. Catal.*, 2015, **324**, 98–106.